Nuclear Instruments and Methods in Physics Research B 531 (2022) 82–92

Contents lists available at ScienceDirect

Nuclear Inst. and Methods in Physics Research, B

journal homepage: www.elsevier.com/locate/nimb

Measured and simulated depth-profiles of fragments induced by 200 MeV/u ^{40}Ar ion beam in copper

Edil Mustafin [a], Peter Katrík [a], Márius Pavlovič [b,*], Helmut Weick [a]

[a] GSI Helmholtzzentrum für Schwerionenforschung GmbH, Planckstraße 1, 64291 Darmstadt, Germany
[b] Faculty of Electrical Engineering and Information Technology, Slovak University of Technology in Bratislava, Ilkovičova 3, 81219 Bratislava, Slovak Republic

ARTICLE INFO

Keywords:
Accelerator
Activation
FLUKA
Fragmentation
Heavy ion
Ion beam

ABSTRACT

This work is a further contribution to our long-term experimental studies of activation- and fragmentation-related effects induced by high-energy heavy-ion irradiation in selected accelerator-construction materials. A stacked-foil copper target consisting of thin foils with different thicknesses was irradiated by 200 MeV/u ^{40}Ar ions. Gamma spectra of the radiation emitted from the activated foils were measured and the nuclides created in the foils as a result of nuclear interaction between the ^{40}Ar ions and the copper target nuclei were identified. The activities of all identified nuclides have been determined from the gamma spectra. The measured activity of each nuclide has been converted to the number of nuclei (of that nuclide) contained in the foil. Finally, the depth-profiles of the induced nuclides, i.e. the number of the induced nuclei as a function of the target depth, have been constructed and analyzed. The measured depth-profiles provide information on physical mechanisms of the high-energy heavy-ion fragmentation. The measured depth-profiles have been also compared with the simulated ones obtained with FLUKA2020. Keeping in mind complexity of the nucleus-nucleus interactions in the broad energy interval, the measured and simulated depth-profiles show a reasonable agreement. However, in some cases, discrepancies between the measured and the simulated depth-profiles have been observed. These cases are presented and discussed in the paper, as they can serve improvement of physical models implemented in the simulation codes.

1. Introduction

Beam transport in accelerators is always accompanied with unavoidable beam losses. The lost beam particles hit the accelerator components, activate the materials these components are made from and/or deteriorate their functional properties [1–6]. Activation of accelerator components is a serious problem especially for high-power heavy-ion machines. Activation and irradiation studies are needed to provide necessary input data for solving radiation protection and components life-time issues [7]. A primary goal of the activation studies is to get quantitative information on induced nuclides and their activities in accelerator-construction materials. Correct identification of the induced nuclides and their activities is of crucial importance for prediction of radiation situation in the vicinity of these machines, hands-on maintenance limits, beam-loss limits, optimization of the machine operation and shut-down cycles, future decommissioning procedures, *etc*.

Activation studies can be based either on dedicated experiments or on computer simulations performed with particle transport codes. Experimental studies are, however, very much limited by available infrastructure and beam time. Special situation comes with newly planned facilities like FAIR (Facility for Antiproton and Ion Research, Darmstadt, Germany, [8–10]) that will be operated with new machine components and at the beam parameters exceeding the ones available during the design phase. In such a case, the activation data can only be gained either by extrapolating (scaling) the data from available experiments or – again – by computer simulations [11,12]. However, due to enormous complexity of heavy-ion nuclear interactions with matter in a broad energy-interval, experimental data are still needed. The experimental data presented in this paper provide information on physical mechanisms of high-energy heavy-ion fragmentation. They are also needed to support development and improvement of physical models implemented in the particle transport codes.

Since 2006, several activation studies have been performed at the SIS18 synchrotron at GSI Darmstadt in the framework of preparation for the FAIR project [13–23]. Most of them dealt with identification of the induced nuclides and determination of their activity for various

* Corresponding author.
E-mail addresses: e.mustafin@gsi.de (E. Mustafin), p.katrik@gsi.de (P. Katrík), marius.pavlovic@stuba.sk (M. Pavlovič), h.weick@gsi.de (H. Weick).

https://doi.org/10.1016/j.nimb.2022.09.022
Received 29 January 2022; Received in revised form 26 September 2022; Accepted 28 September 2022
Available online 10 October 2022

combinations of beam particles, beam energy, target materials, and target shape (bulky stacked-foil configuration or pipe-like geometry). At that occasion, comparison between the measured and simulated data was performed. While a good agreement was found between the measured and simulated ranges [20,23], discrepancies have been observed between the measured and simulated depth-profiles of induced activity. That is why we have decided to continue with studies collecting data from irradiation experiments and comparing them with results from particle transport codes commonly used to simulate effects related to interaction of high-energy heavy-ion beams with matter. In most our works, we used FLUKA. One experiment included also SHIELD-A, MARS15, GEANT4 and PHITS. Our previous experiments are going to be described briefly in the next section.

In the recent experiment presented in this paper, a stacked-foil copper target (natural mixture of ^{63}Cu and ^{65}Cu isotopes) assembled from thin foils has been irradiated with 200 MeV/u fully-stripped ^{40}Ar projectiles. Depth-profiles of ^{7}Be, ^{22}Na, ^{46}Sc, ^{54}Mn, ^{56}Co, ^{57}Co, ^{58}Co, ^{60}Co, and ^{65}Zn have been investigated and simulated with FLUKA2020 [24–27]. The measured depth-profiles are compared with the simulated ones. The level of agreement is evaluated using the C/M ratio (the ratio between the calculated and the measured values) for all measured points of a depth-profile. Attention is paid especially to cases when the simulated and the measured depth-profiles deviate from each other. These discrepancies are discussed in this paper. Nuclides heavier than copper, ^{75}Se, ^{83}Rb, ^{88}Y, and ^{88}Zr have been observed, too. They were detected in two foils only without having a real depth-profile. That was why they were not simulated.

2. Materials and methods

2.1. Choice of the experimental conditions

2.1.1. Previous studies

The choice of the experimental conditions has been very much based on our experience from previously conducted activation studies and similar works published in the literature [28]. Ref. [17] reports on a benchmark test of FLUKA for activation of copper and stainless steel targets with 950 MeV/u and 500 MeV/u uranium beams. In that work, the simulations were performed with FLUKA2006.3b. FLUKA was used with defaults NEW-DEFA and no further energy or particle cut-offs were set. The simulated and measured activities of the induced nuclides were mutually compared. The activities were obtained by integration of the simulated and measured activity depth-profiles. It means, they represented the global induced activities in the target regardless of the depth distribution. The agreement was better for the target fragments compared to the projectile fragments. In case of the target fragments, the worst ratio (measured-to-simulated) was 3.2 for ^{22}Na in the copper target irradiated by 950 MeV/u uranium beam. In case of the projectile fragments, it was 10.5 for ^{237}U, again in the copper target irradiated by 950 MeV/u uranium beam. Further interesting result concerned sensitivity to the implemented physical models in FLUKA. For example, an upgrade of the model for evaporation of light fragments improved the ratio for ^{7}Be from 6 to 2.5 [17]. A similar result was observed for several other nuclides in both targets. Generally, for most of the target fragments, the mismatch ratio (measured-to-simulated as well as simulated-to-measured) was <2. It shall be noticed that the target fragments represent the dominant contribution to activation of the accelerator-construction materials [16].

Next studies dealt with lighter projectiles (1 GeV/u and 500 MeV/u argon ions in copper [18]), additional target materials (430 MeV/u and 500 MeV/u argon ions in aluminum [19]), and lower energies (200 MeV/u uranium ions in aluminum [21]; 125 MeV/u, 200 MeV/u uranium ions and 300 MeV/u xenon ions in aluminum [22]). Results published in Ref. [18] are basically consistent with the previous study [17]. The measured-to-simulated global activity ratio was <1.6 at both energies. In most cases (except for ^{56}Co and ^{57}Co), FLUKA gave lower activities than the measured ones. To some extent, the shapes of the measured and simulated activity depth-profiles were compared, too. While FLUKA reproduced the profile shape quite well, the absolute activity values differed (i.e. the measured and simulated profiles were vertically shifted with respect to each other). However, it must be pointed out that the target configuration in that experiment was not optimized for high depth resolution. The target consisted of thin activation foils (0.5 mm) separated by thicker spacers (7 mm and 15 mm at 500 MeV/u and 1 GeV/u, respectively). The only exception was the projectile-range region of the target where several activation foils without the spacers were stacked together.

The study reported in Ref. [19] used 430 MeV/u and 500 MeV/u argon beams in aluminum targets. In this reference in addition FLUKA2008.3b, MARS15 [29–33], GEANT4 [34,35], PHITS [36] and SHIELD-A [37] were also subject to validation, similarly to the work published in Ref. [38]. All investigated simulation codes showed some discrepancies with respect to the measured data (that were taken as the reference data even if they were inevitably accompanied by uncertainties). This uncertainty was 10.2% in reference [38]. According to the data analysis presented in that work, 77% (on average, from 71% to 86% depending on the code) of evaluated data points were in the C/M interval from 0.7 to 1.3. But each code showed also some anomalous results for certain nuclear reaction at certain energy. C/M values up to 14.5 are reported in [38]. A prevailing tendency – but not a general rule – was that the codes underestimated the measured values and the largest deviations were observed at low (in that case proton) energies. Our studies [19,21,22] brought similar results also for much heavier projectiles.

In order to get more detailed information and closer view especially on the observed discrepancies between the simulated and measured depth-profiles, we have recently run and analyzed a dedicated experiment with enhanced depth-resolution of the target. Results of this experiment are presented in this paper.

2.1.2. The target

The enhanced depth-resolution has been achieved by stacking together many thin activation foils without spacers between them. The target material was copper (natural mixture of ^{63}Cu and ^{65}Cu, purity higher than 99.95% according to the specification of the manufacturer). The target body was assembled from 70 square activation foils 10 $\times$ 10 cm each. The geometry (the order-number and thickness of the foils) is listed in Table 1. The overall length of the target was 13 mm. After the irradiation of the whole target (and cooling time of about 4 months), the gamma-spectroscopic analysis of the individual target foils has been launched. However, in order to shorten the gamma-spectra acquisition time as well as to improve the statistics of the measured spectra, few foils have been grouped and measured together. This is also indicated in Table 1. Grouping the foils is a trade-off between the measurement time, data quality and depth resolution. More foils provide higher cumulated activity (consequently shorter measurement time and better statistics), but worse depth resolution. Grouping the foils can be used in those regions of the depth-profiles where the depth resolution is not of crucial importance.

2.1.3. Irradiation conditions

The choice of the initial beam energy (200 MeV/u) was primarily determined by the fact that in the previous studies, major discrepancies between experimental results and simulations were reported mostly at low energies. As the 200 MeV/u beam penetrates through the target, it is slowed down passing 125 MeV/u which is the energy when FLUKA switches from the RQMD (Relativistic Quantum Molecular Dynamics) to the BME (Boltzmann Master Equation) model. It is interesting to investigate whether such a transition can be recognized in the simulated depth-profiles. Finally, the chosen energy also corresponds well to the energies used at the future SIS100 synchrotron. The injection energy to the SIS100 (=extraction energy from the SIS18) is going to be 200 MeV/

Table 1
Configuration of the copper target irradiated by the 200 MeV/u ^{40}Ar beam. The foils are numbered from the beam-facing side of the target and their grouping for the gamma-spectroscopic measurements is indicated, too. The grouping corresponds to the first set of measurements (see section 2.3.2). In the second set of activity measurements, some groups were split into individual foils. The foil thicknesses are quoted according to the specification of the manufacturer. In all numerical calculations as well as in FLUKA simulations, the copper density of 8.96 g/cm^3 was used.

Foil order-number	1–4	5–6	7–8	9–10
Foil thickness [mm/foil]	0.5	0.2	0.2	0.2
Gamma-spectroscopy	Individually	Grouped	Grouped	Grouped
Group number	1–4	5	6	7
Foil order-number	11–12	13–14	15–16	17–18
Foil thickness [mm/foil]	0.2	0.2	0.1	0.1
Gamma-spectroscopy	Grouped	Grouped	Grouped	Grouped
Group number	8	9	10	11
Foil order-number	19–20	21–23	24–33	34–41
Foil thickness [mm/foil]	0.1	0.1	0.05	0.1
Gamma-spectroscopy	Grouped	Individually	Individually	Individually
Group number	12	13–15	16–25	26–33
Foil order-number	42–43	44–46	47–49	50–51
Foil thickness [mm/foil]	0.1	0.1	0.1	0.2
Gamma-spectroscopy	Grouped	Grouped	Grouped	Grouped
Group number	34	35	36	37
Foil order-number	52–53	54–55	56–57	58–59
Foil thickness [mm/foil]	0.2	0.2	0.2	0.2
Gamma-spectroscopy	Grouped	Grouped	Grouped	Grouped
Group number	38	39	40	41
Foil order-number	60–61	62–63	64	65
Foil thickness [mm/foil]	0.2	0.2	0.2	0.5
Gamma-spectroscopy	Grouped	Grouped	Grouped	
Group number	42	43	44	
Foil order-number	66–67	68–70		
Foil thickness [mm/foil]	0.5	0.5		
Gamma-spectroscopy	Grouped	Grouped		
Group number	45	46		

u. Since extraction/injection is always accompanied with higher beam losses, it is important to collect data especially at those energies.

The choice of the target material (copper) bears also some relation to the beam losses. There are serious vacuum-induced losses due to charge-stripping of the beam particles by the residual gas. The ions with the altered charge-state have consequently wrong rigidity and follow a wrong orbit, which leads to their loss. Those losses are considered to be the controlled losses and will be absorbed by special cryocatchers made of copper [39].

The irradiation was performed at GSI HHD cave, where the target was mounted on a movable platform in front of the extraction beam-dump of the SIS18 synchrotron. The target was moved away from the beam before and after the irradiation. A beam spot of about 3 cm × 4 cm was estimated with the aid of a scintillator screen installed on the same movable platform as the target and used for beam adjustment before the irradiation. A beam intensity of every single beam-pulse in the fast-extraction regime was recorded over the whole irradiation time with uncertainty of about 3%. The irradiation time was 4 h, 6 min and 45 s. During this irradiation time, a total number of 1.03×10^{13} ions was accumulated. The most important experimental conditions are summarized in Table 2.

2.2. Computer simulations

Two features of FLUKA are important to be mentioned in relation to modeling of our experiment. First, it is very important that FLUKA – in contrast to some other codes – calculates not only production rates but also the time-evolution of activity of the nuclides of interest. This calculation takes automatically into account all possible production channels of the nuclide of interest without requiring any intervention from the user. In some cases, the nuclide produced at first directly at a fragmentation event is not the nuclide of interest detected after the cooling time, but a nuclide that decays to it. This can lead to a presence of shorter lived gamma emitters, even after a long cooling time after the end of irradiation, like in the case of ^{60}Fe ($T_{1/2} = 2.6$ My) and ^{60}Co ($T_{1/2} = 5.3$ y). Following their activity as a function of time is impossible because the activity of the parent cannot be determined by gamma spectroscopy. But as lifetimes and expected production rates are so different it does not pose a real problem in the presented data.

Second, nuclear interactions induced by ions are treated in FLUKA through interfaces to different external energy-dependent event generators:

- Above 5 GeV/u: DPMJET-II or DPMJET-III, with special initialization procedure;
- From 0.125 GeV/u to 5 GeV/u: modified RQMD (Relativistic Quantum Molecular Dynamics);
- Below 0.125 GeV/u: BME (Boltzmann Master Equation).

Our results show that the transition from RQMD to BME is not smooth and suffers from some artificial irregularities present in some of the simulated depth-profiles of the nuclide foil-abundancies. The worst case has been observed for ^{7}Be. The present simulations have been run with the following FLUKA settings (consult the FLUKA manual for further details [41]):

- DEFAULTS: NEW-DEFA;
- Three PHYSICS cards were activated:

Table 2
A summary of the main experimental conditions. ATIMA stands for an energy-loss and ion-range calculation computer program used to calculate the ranges and energy-to-depth curves in this work [40], see also Section 3.2.

The target	
Target material:	Natural mixture of ^{63}Cu and ^{65}Cu
Number and dimensions of the activation foils:	70, 10 × 10 cm squared, variable thickness
Total target thickness:	13 mm
Irradiation conditions	
Ion species:	$^{40}Ar^{18+}$
Ion energy (in front of the vacuum window):	200 MeV/u
Ion energy (on the target surface):	195.55 MeV/u
Duration of the irradiation:	4 h 6 min 45 s (14805 s)
Beam spot on the target:	3 cm × 4 cm
Total number of ions accumulated on the target:	1.03×10^{13}
Residual range of $^{40}Ar^{18+}$ in the target (ATIMA):	5.165 mm ± 0.01 mm (range straggling)
Range uncertainty, taking into account ATIMA and matter-thickness accuracy:	~0.1 mm

- o EVAPORAT: New evaporation model with heavy fragments;
- o COALESCE: Coalescence ON;
- o EM-DISSO: Target and projectile electromagnetic dissociation: ON;
- IONTRANS card: HEAVYION.

The simulations included the vacuum window (100 μm stainless steel), the 60 cm air gap between the vacuum window and the target surface, and the target itself. The FLUKA simulations followed the experiment also from the timing point of view, which is important for consistency between the simulated and experimental data that are both quoted at the time-point of the end of irradiation. The FLUKA results were calculated including the cooling time and then extrapolated backwards to the end of irradiation.

2.3. Gamma spectroscopy

2.3.1. Spectroscopic chain

The gamma-ray spectra were measured by a coaxial high-purity germanium detector with the energy range from 40 keV up to 1.9 MeV. Energy and efficiency calibrations were done at the beginning of each set of activity measurements with the following set of calibration sources and energy-lines: ^{241}Am (59.54 keV), ^{109}Cd (88.04 keV), ^{57}Co (122.06 keV, 136.47 keV), ^{139}Ce (165.86 keV), ^{113}Sn (391.69 keV), ^{85}Sr (514.01 keV), ^{137}Cs (661.66 keV), ^{88}Y (898.04 keV, 1836.06 keV), and ^{60}Co (1173.24 keV, 1332.50 keV). The calibration sources consisted of 7 drops arranged equidistantly on the round flat surface with diameter of 3 cm, one drop in the center and 6 drops around it. The calibration source was located 7 cm above the surface of the aluminum detector-crystal cap. The spectra of all foils were measured in the same geometry, i.e. 7 cm above the surface of the detector-crystal cap. The beam spot was elliptic about 3 × 4 cm (horizontally × vertically). Standard built-in GammaVision routines for the energy and efficiency calibration were used. The resulting efficiency calibration curves for the two calibrations corresponding to the two sets of activity measurements are shown in Fig. 1. The fitting function for an efficiency calibration curve has the form:

$$Efficiency = exp\left(c_1 E + c_2 + \frac{c_3}{E} + \frac{c_4}{E^2} + \frac{c_5}{E^3} + \frac{c_6}{E^4}\right) \quad (1)$$

where E is the photon energy in MeV and c_i are the fitting coefficients provided by GammaVision. The uncertainty of the activity measurements of the calibration sources was better than 3.7% (detailed data saved for the second calibration only). The fitted efficiency calibration curves deviate from the measured points by few percent.

There were few weeks break between the first and the second set of measurements (see Section 2.3.2). During the break, the detector underwent a regular maintenance and conditioning including exchange of its preamplifier. After the maintenance, at the beginning of the second set of measurements, the detector was re-calibrated. An improved efficiency in the region from ≈100 keV to ≈400 keV (see Fig. 1) accompanied with a slight rise of the background electronic noise below 120 keV was observed. The maximum relative improvement of the efficiency is 17% at 240 keV.

Fig. 2 shows the energy calibration data that exhibit expected linearity (the correlation coefficient for the linear fit is 0.9999999830 and 0.9999999871 for the first and the second calibration, respectively). The energy-per-channel increment is 0.116 eV/channel.

Fig. 3 shows the energy resolution in terms of the peak FWHM (Full Width at Half Maximum) as a function of the photon energy together with a second-order polynomial fit. The correlation coefficient is 0. 9981 and 0.9974 for the first and the second calibration, respectively.

Standard GammaVision routines were used for the energy and efficiency calibrations. The energy calibration exhibits almost perfect linearity. The efficiency calibration curve in the form of Eq. (1) deviates from the individual measured calibration points by few percent. The major contribution to the absolute efficiency uncertainty comes from the uncertainty of measured activities of calibration sources. This uncertainty ranged from 0.3% up to 3.7% for the second calibration measurement. The calibration and the sample measurements were performed exactly in the same geometry (the calibration source and the activated foil 7 cm above the aluminum detector-crystal cap) and the dimensions of the calibration sources were comparable with the activated part of the samples. The spectra were processed with the aid of the ROI32 GammaVision procedure that takes into account the background and yields the resulting statistical uncertainties of the measured activities.

2.3.2. Activity measurements and data processing

The gamma-ray spectra were measured in a low-background chamber. In order to distinguish between short-lived and long-lived nuclides as well as to increase the measurement accuracy, the gamma-ray spectra were recorded in two sets of measurements at different time points after the end of irradiation. The irradiation was performed in February 2020. The first set of measurements started in June 2020 and lasted till September 2020. It was followed by recalibration and background measurements. The second set of measurements started in September 2020 and lasted till June 2021. In the second set of measurements, each

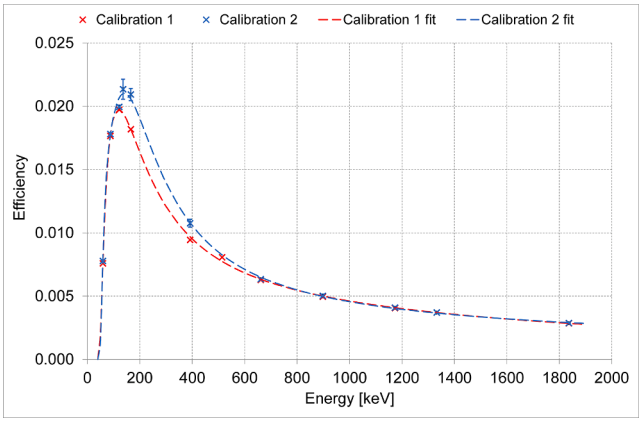

Fig. 1. Efficiency calibration curves of the spectroscopic chain. The two calibrations correspond to the two sets of activity measurements. Efficiency calibration was done at the beginning of each set of activity measurements. The error bars indicate the uncertainty of the activity measurements of the calibration sources (detailed data saved for the second calibration only).

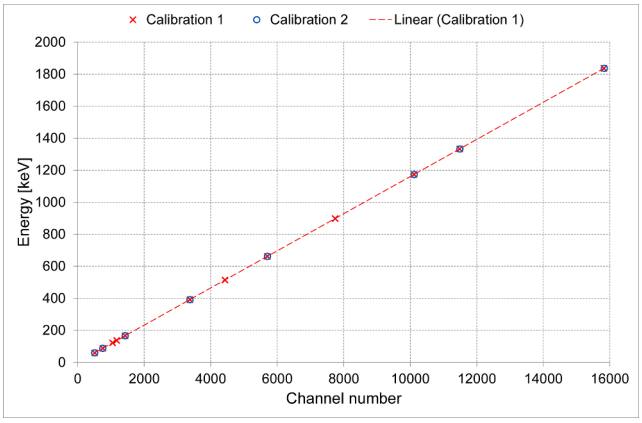

Fig. 2. Energy calibration of the spectroscopic chain. The two calibrations correspond to the two sets of activity measurements. Energy calibration was done at the beginning of each set of activity measurements together with the efficiency calibration. The trend lines are practically identical for both energy calibrations. That is why only one of them is displayed in the plot.

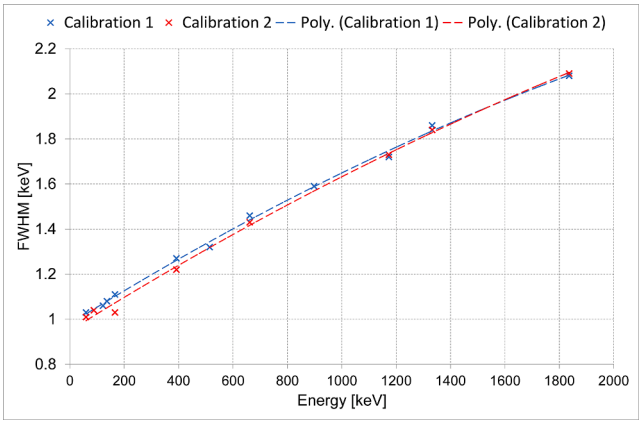

Fig. 3. Energy resolution in terms of the peak FWHM (Full Width at Half Maximum) of the spectroscopic chain as a function of the photon energy. The two data sets correspond to the two sets of activity measurements.

group of foils was measured about twice longer than in the first set. Data-acquisition time for one gamma spectrum fluctuated from several hours up to few days, depending on the activity of the measured foil. Further measurement optimization was done by measuring several foils together as a group (see Table 1), which is a trade-off between the measured activity and the depth resolution. A group consisting of several foils provides higher activity which means better statistics and higher signal-to-noise ratio, but lower depth resolution.

Because the activities of individual foils are measured at different time-points, they must be brought to a common reference time-point in order to construct a depth-profile. Consistently with our previous works [14,15,18,19,21,22], the end of irradiation was selected as the reference time-point. Therefore, the activities determined from each measurement set were extrapolated to the end of irradiation. A simple one-decay exponential decay-law has been used for this purpose. In case of a decay chain, it is an approximation only. Some nuclides of interest measured after the cooling time may be a daughter of an unstable parent that is produced by the primary projectile – target-nucleus collisions (for example FLUKA predicts about 10% contribution to ^{22}Na from beta decay of ^{22}Mg). Unfortunately, the contribution from this indirect production channel cannot be resolved from activation data measured after the cooling time we used (≈ 4 months). On the other hand, the half-life of the parents is much shorter than the cooling time. That is why we have made an approximation like the parent nuclei decayed immediately at the end of irradiation. As a consequence, they are counted together with the nuclei of interest in the extrapolated data.

The same is true for metastable nuclides. The isomers are not distinguishable any more after the cooling time. However, among the identified nuclides (see the next section), the ^{58m}Co has the longest half-life of 9.04 h, which is still much shorter than the cooling time. Other possible metastable nuclides ^{46m}Sc and ^{60m}Co have the half-live of 18.75 s and 10.47 min, respectively. We have compared analytically the decay curves for ^{58}Co starting from: (1) 100% abundance of ^{58}Co, and (2) 50% abundance of ^{58}Co plus 50% abundance of ^{58m}Co. They converge together in about two days. It must be pointed out that the same approach has been applied to both, the experimental as well as the simulated data. The FLUKA simulations were run including the cooling time and extrapolated back to the end of irradiation in the same manner as the experimental data. This eliminates inconsistency between the experiment and the simulations caused by the approximation we made.

In the measured and simulated depth-profiles presented in the following section, the extrapolated activities are converted to the number of radioactive nuclei of the nuclide of interest contained in the foil. The conversion is based on the proportionality between the activity and the number of radioactive nuclei via the decay constant. These nuclide foil-abundancies are normalized per one incident projectile and per unit thickness of 1 mm. They are always assigned to the depth-coordinate corresponding to the position of the middle of the foil (or the middle of the foil group) starting from zero at the target surface. For example, the first data point has its depth-coordinate 0.25 mm since the first foil is 0.5 mm thick.

3. Results and discussion

3.1. Identified fragments

Thirteen nuclides were detected, identified, and analyzed. They are collected in Table 3. Further nuclides, namely ^{49}V, ^{51}Cr, and ^{59}Fe were also detected, but their activities were too low for reliable reconstruction of the depth-profiles. As an example, a measured depth-profile of ^{59}Fe is shown in Fig. 4. The profiles of ^{49}V and ^{51}Cr were even worse.

The nuclides ^{75}Se, ^{83}Rb, ^{88}Y, and ^{88}Zr (all heavier than ^{65}Cu) were detected in two foils only, so reconstruction of their depth-profiles made no sense. However, this specific feature is very interesting since it can be used as a tool to identify the range-foil, which has been mentioned already in our previous work [23]. We are going to collect data from several experiments and to analyze this range-determination technique in a separate paper. Other nuclides from Table 3 were detected in all target foils.

3.2. The energy-to-depth curves

In order to assist interpretation of the results, the depth-profiles presented in the following section are equipped with an energy-to-depth curve as supporting information. It should be noted that the Ar beam passes through a vacuum window (100 μm stainless steel) and 60 cm of air before hitting the copper target. That is why its energy on the target surface is 195.55 MeV/u according to ATIMA calculation [40], rather than 200 MeV/u. The projectile kinetic energy drops to zero at the target depth representing the residual range of the Ar beam in the copper target (5.165 mm, again according to ATIMA).

The energy-to-depth curve can have two types of branches. In Fig. 5 the left, decreasing branch (black curve) corresponds to the energy of an ^{40}Ar^{18+} projectile at which a fragmentation event happens as a function of the target depth. Note that we are talking only about the fragmentation events induced by the primary projectiles, not by the secondary particles. This fragmentation event may result in production of a target fragment as well as a projectile fragment. While the target fragments are assumed to stay approximately at the location where they have been generated, the projectile fragments continue moving preferably in the projectile direction with velocity approximately identical to the projectile velocity. The stopping depth of the projectile fragments in the target can then be determined as the depth of the fragmentation event plus the projectile-fragment range. This is the way how the right (increasing) branches of the energy-to-depth curve in Fig. 5 have been constructed. The calculations were done with ATIMA neglecting a small energy change in the fragmentation event itself.

The right, the projectile-fragment branches are fragment-specific. There are only two possible candidates for projectile fragments among the identified nuclides, namely ^{7}Be, the red curve in Fig. 5, and ^{22}Na, the blue curve in Fig. 5. A numerical example is given for a ^{22}Na generated at the kinetic energy of 159.4 MeV/u. Its stopping depth can be read on the ^{22}Na blue curve at 159.4 MeV/u.

3.3. Measured and simulated depth-profiles

Figs. 6–14 systematically show the activation depth-profiles of identified nuclides together with the profiles obtained by the Monte Carlo transport code FLUKA. Two measured profiles are shown for each nuclide corresponding to the first and to the second set of the activity measurements. The only exception is ^{7}Be for which only the data from the first set of measurements are available due to its short half-life. The

Table 3
Identified and analyzed nuclides, their half-lives (d – days, y – years), photon energies in the photo-peaks identified in the measured spectra and their abundancies.

Nuclide	Half-life	Energy [keV]	Abundance [%]	Nuclide	Half-life	Energy [keV]	Abundance [%]
^{7}Be	53.22 d	477.61	10.390	^{60}Co	5.2712 y	1173.24	99.974
						1332.50	99.986
^{22}Na	2.6018 y	1274.53	99.944	^{65}Zn	243.93 d	1115.55	50.600
^{46}Sc	83.79 d	889.28	99.984	^{75}Se	119.78 d	121.12	17.140
		1120.55	99.987			136.00	58.300
						264.66	58.500
						279.54	24.790
						400.66	11.370
^{54}Mn	312.20 d	834.85	99.976	^{83}Rb	86.2 d	520.49	44.700
						529.64	29.300
						552.63	16.000
^{56}Co	77.236 d	846.77	100.000	^{88}Y	106.626 d	898.04	93.700
		1037.84	14.140			1836.06	99.200
		1238.28	66.070				
		1771.35	15.480				
^{57}Co	271.74 d	122.06	85.600	^{88}Zr	83.4 d	392.87	97.290
		136.47	10.680				
^{58}Co	70.86 d	810.78	99.448				

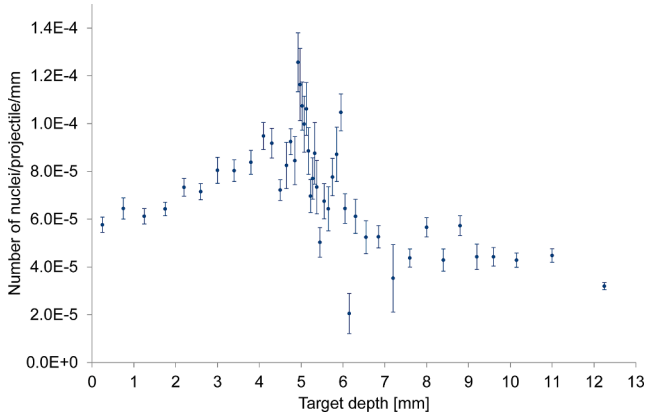

Fig. 4. Depth-profile of ^{59}Fe from the first set of measurements. Low activity leads to poor statistics manifested by large uncertainties. This kind of profiles was excluded from further analysis.

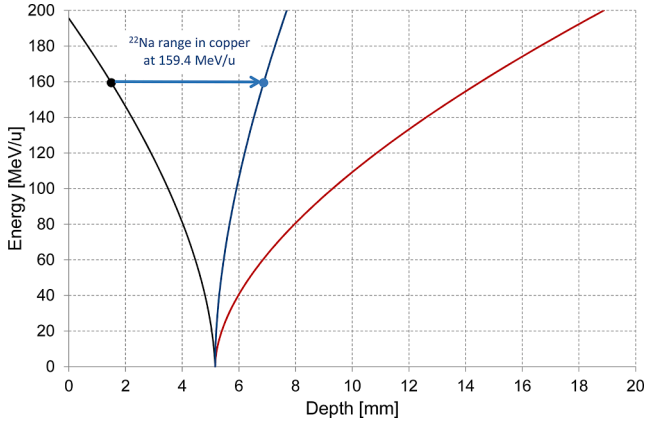

Fig. 5. The energy-to-depth curves including fragmentation: black – $^{40}Ar^{18+}$ projectiles, blue – ^{22}Na fragments, red – ^{7}Be fragments. (For interpretation of the references to colour in this figure legend, the reader is referred to the web version of this article.)

measured activities are converted into the number of radioactive nuclei of the nuclide of interest and normalized per unit thickness (1 mm) and per one incident projectile. The conversion is based on proportionality between the activity and the number of radioactive nuclei via the decay

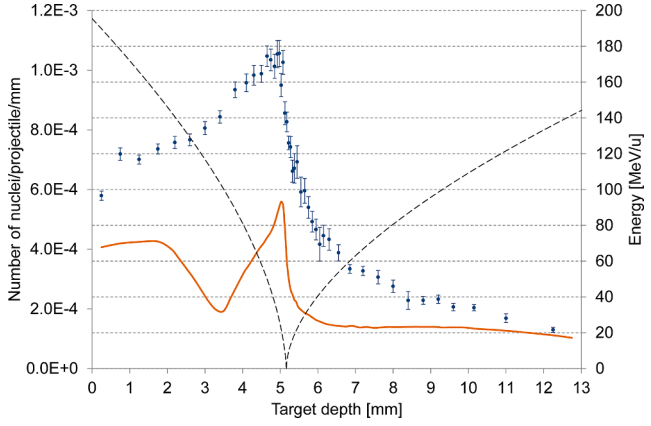

Fig. 6. Measured and simulated ^{7}Be profiles. Blue data points – the first measured profile, orange line – the FLUKA-simulated profile, black dashed line – the energy-to-depth curve. The error bars represent statistical uncertainties provided by GammaVission. (For interpretation of the references to colour in this figure legend, the reader is referred to the web version of this article.)

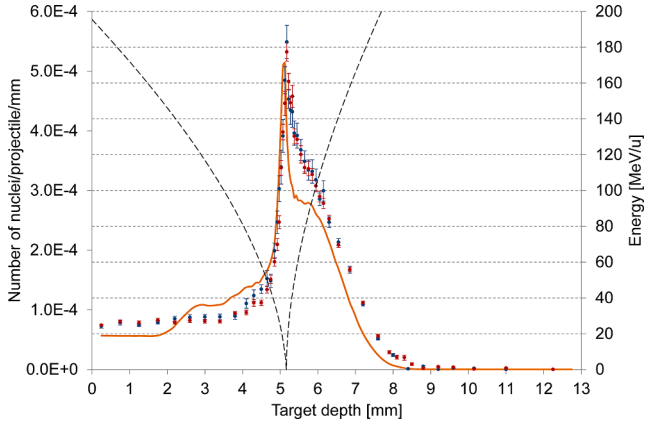

Fig. 7. Measured and simulated ^{22}Na profiles. Blue data points – the first measured profile, red data points – the second measured profile, orange line – the FLUKA-simulated profile, black dashed line – the energy-to-depth curve. The error bars represent statistical uncertainties provided by GammaVission. (For interpretation of the references to colour in this figure legend, the reader is referred to the web version of this article.)

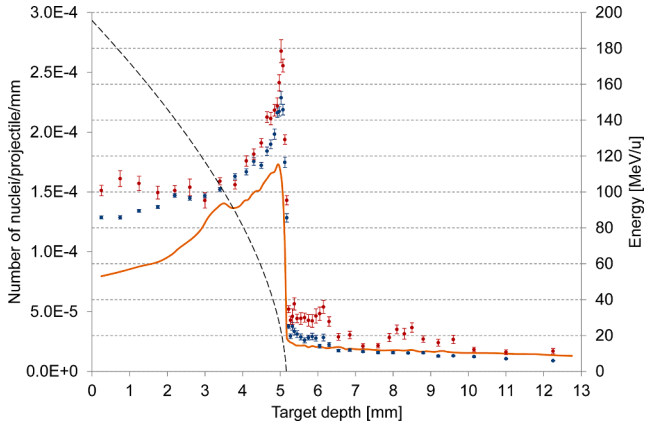

Fig. 8. Measured and simulated ^{46}Sc profiles. Blue data points – the first measured profile, red data points – the second measured profile, orange line – the FLUKA-simulated profile, black dashed line – the energy-to-depth curve. The error bars represent statistical uncertainties provided by GammaVission. (For interpretation of the references to colour in this figure legend, the reader is referred to the web version of this article.)

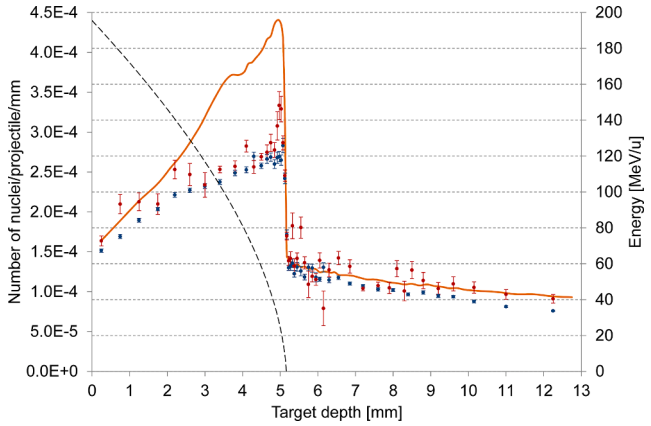

Fig. 10. Measured and simulated ^{56}Co profiles. Blue data points – the first measured profile, red data points – the second measured profile, orange line – the FLUKA-simulated profile, black dashed line – the energy-to-depth curve. The error bars represent statistical uncertainties provided by GammaVission. (For interpretation of the references to colour in this figure legend, the reader is referred to the web version of this article.)

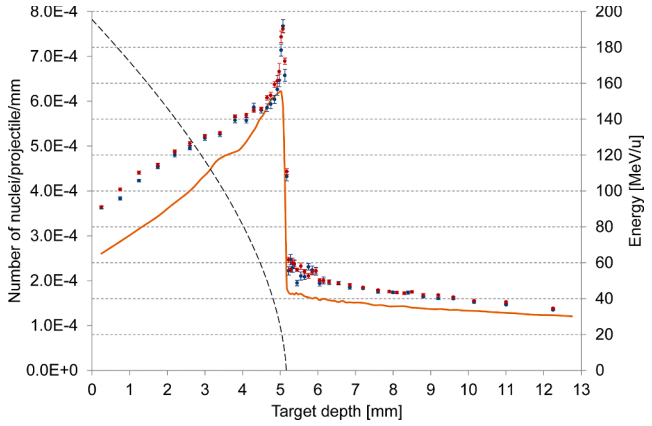

Fig. 9. Measured and simulated ^{54}Mn profiles. Blue data points – the first measured profile, red data points – the second measured profile, orange line – the FLUKA-simulated profile, black dashed line – the energy-to-depth curve. The error bars represent statistical uncertainties provided by GammaVission. (For interpretation of the references to colour in this figure legend, the reader is referred to the web version of this article.)

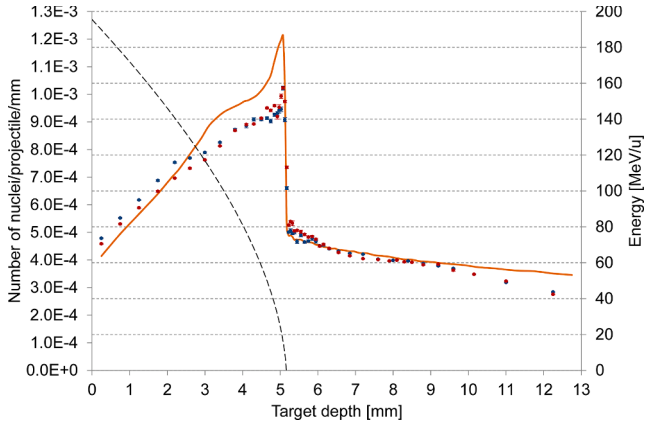

Fig. 11. Measured and simulated ^{57}Co profiles. Blue data points – the first measured profile, red data points – the second measured profile, orange line – the FLUKA-simulated profile, black dashed line – the energy-to-depth curve. The error bars represent statistical uncertainties provided by GammaVission. (For interpretation of the references to colour in this figure legend, the reader is referred to the web version of this article.)

constant. The statistical uncertainties of the FLUKA data are comparable with the line thickness used for the FLUKA profiles. They are typically ≈ 0.5% (≈ 1% in the tails behind the projectile range).

3.3.1. *Beryllium-7*

The measured and simulated depth-profiles of ^{7}Be are shown in Fig. 6.

Upstream of the projectile range, the measured ^{7}Be profile is a typical target-fragment profile increasing from the target surface till the projectile-range foil at 5.165 mm. Downstream of the range, it exhibits a long tail caused by superposition of the target activation from secondary particles produced from the projectile with a longer range, and implanted radioactive fragments of the ^{40}Ar projectile which also have a longer range, see Fig. 2. An independent simulation with the MOCADI code [42] for simulation of beamlines with matter, including ATIMA but for projectile fragments only, shows for depth larger than 7 mm a distribution very similar to FLUKA also in quantity. The ^{7}Be projectile fragments generated at the target surface (or even in the vacuum window and air in front of the target) have residual range in the target up to 18.9 mm. Since the experimental data are cut off at 12.25 mm, it is not possible to distinguish clearly between the projectile-fragment and target-fragment contributions behind the Ar range. They both can have a sizeable share. A minimum of activation left of the peak like predicted by FLUKA is not visible. It occurs just at the transition region from the RQMD to the BME model in FLUKA.

The observed lower activity in the first foil compared to the following ones is not expected by theory [43], but it exceeds 1σ statistical effects. It is likely a statistical fluctuation of the first and the second points of the measured profile exceeding the 1σ error bars.

3.3.2. *Sodium-22*

The measured and simulated depth profiles of ^{22}Na are shown in Fig. 7.

The ^{22}Na profile combines two features. Upstream of the projectile range, it is a target-fragmentation profile. Up to the depth of about 4 mm, the profile is almost constant. This indicates that the ^{22}Na nuclei are generated practically only by direct collisions of the projectiles with the target nuclei, but not by collisions of secondary particles with the target nuclei. Obviously, the secondary particles are not energetic enough to break the copper nuclei down to ^{22}Na. The depth of 4 mm corresponds to

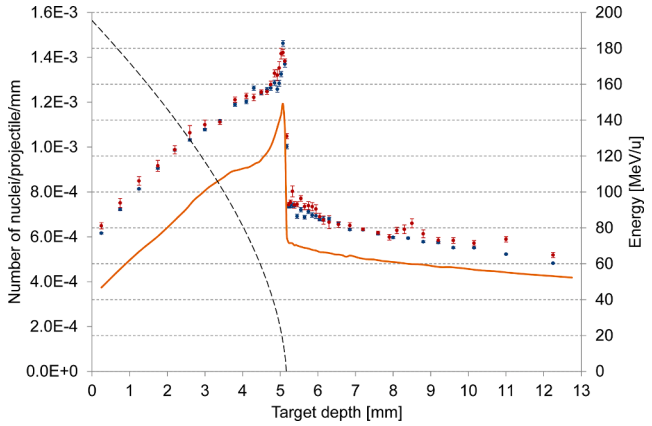

Fig. 12. Measured and simulated ^{58}Co profiles. Blue data points – the first measured profile, red data points – the second measured profile, orange line – the FLUKA-simulated profile, black dashed line – the energy-to-depth curve. The error bars represent statistical uncertainties provided by GammaVission. (For interpretation of the references to colour in this figure legend, the reader is referred to the web version of this article.)

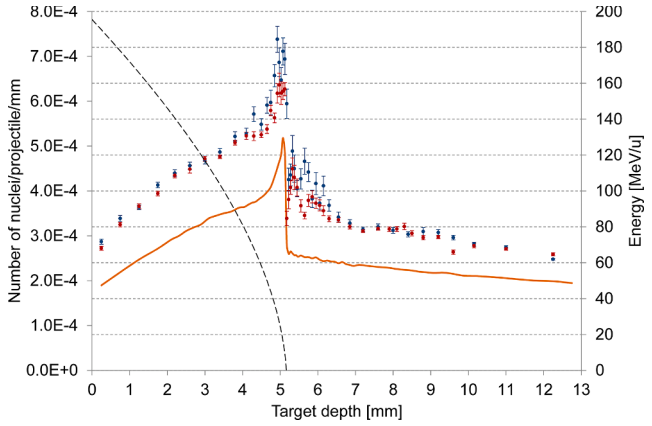

Fig. 13. Measured and simulated ^{60}Co profiles. Blue data points – the first measured profile, red data points – the second measured profile, orange line – the FLUKA-simulated profile, black dashed line – the energy-to-depth curve. The error bars represent statistical uncertainties provided by GammaVission. (For interpretation of the references to colour in this figure legend, the reader is referred to the web version of this article.)

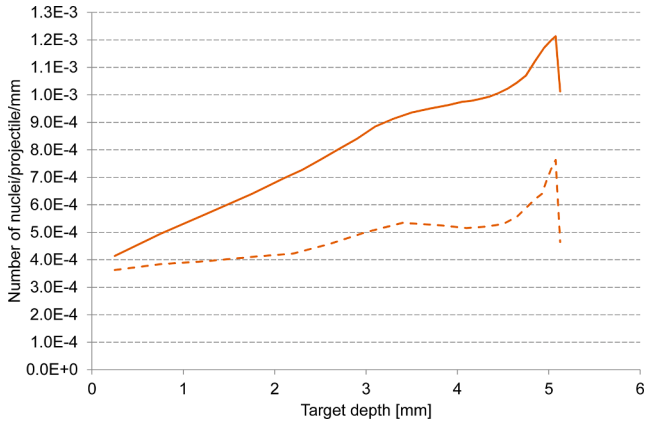

Fig. 14. Comparison of the ^{57}Co profiles in case of the stacked-foil target geometry (solid curve) and individual isolated foils (dashed curve). The activation of the isolated foils was simulated with the ^{40}Ar energy corresponding to the depth-position of the foil in the stacked-foil target.

energy of about 80 MeV/u.

Downstream of the projectile range, it is a typical projectile-fragmentation profile with rather sharp decrease behind the range foil. By its mean atomic stopping range, the ^{22}Na is supposed to stop at a depth of 7.8 mm. However, in addition the momentum spread of the fragmentation reaction must be considered (see [44]) which can also cause acceleration. As faster ions are also slowed down less, this also shifts the mean value in the activation profile to longer ranges. A MOCADI simulation using momentum transfer according to Fermi momentum and a small energy loss in reaction according to [44] shows the extrapolated drop at 8.1 mm. Experiment values show it at about 8.0 mm and FLUKA a bit shorter but of the same shape. At larger depth the ^{22}Na activity dropped below minimum detectable activity. This supports the interpretation that there is practically no contribution from the target fragmentation induced by secondary particles, which would expand deeper.

The height of the peak at the end of the Ar range is well reproduced by FLUKA also with a shoulder towards longer ranges. FLUKA predicts a 10% contribution to ^{22}Na by beta decay of ^{22}Mg which until the activation measurement has practically all decayed to ^{22}Na. It has a very similar activation profile as ^{22}Na.

3.3.3. *Nuclides from Scandium-46 to Cobalt-60*

Nuclides from ^{46}Sc to ^{60}Co are going to be treated in a common section. Their measured and simulated depth-profiles are shown in Figs. 8–13.

These profiles exhibit three typical features of the target-fragmentation profiles. First, a steady increase from the target surface up to the projectile range of 5.17 mm. Unlike the ^{22}Na profile that is almost constant up to about 4 mm, this steady increase is caused by a building-up number of secondary particles that contribute to the target activation.

This can be also demonstrated by the FLUKA simulation. In Fig. 14, an example is given for ^{57}Co. Two curves are shown. One curve corresponds to the ^{57}Co profile in case of the stacked-foil target assembly. The other curve represents the ^{57}Co foil-abundance simulated in individual isolated foils at the ^{40}Ar energy identical to the energy inside the stacked-foil target at the given depth. Naturally, the first and the second simulations differ from each other by the presence of the secondary particles. While in the first case (the stacked-foil target) the secondary particles do contribute to the target activation, they are missing in the simulation with individual isolated foils.

The second characteristic feature in Figs. 8–13 is the sharp drop immediately behind the projectile range. This is caused by the fact that most of the Ar projectiles survive until being stopped. Also many very intense projectile fragments stop in the projectile-range region and do not penetrate deeper. That is why they do not contribute to the target activation downstream of the range.

Finally, there is a long profile tail downstream of the range. This is due to the target activation by light projectile fragments and secondary particles (mostly protons and neutrons) that can penetrate considerably deeper than the projectiles. They follow approximately a gradually attenuating flux with depth.

The fragmentation process of both target and projectile can be well understood by the abrasion ablation model [45]. But to act as practically individual nucleons, large velocity is required which leads to a small de Broglie wave length. This is not the case for lower energies and collective effects become more important. This also means the reaction mechanism and cross section will change significantly. FLUKA treats this in the BME model.

3.3.4. *Zinc-65*

The measured and simulated depth profiles of ^{65}Zn are shown in Fig. 15.

The ^{65}Zn nuclide represents the target reaction products with atomic number, Z, one higher than the atomic number of the Cu-target nuclei.

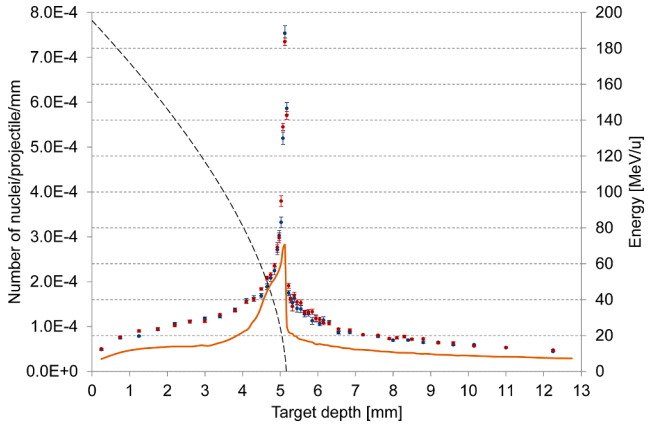

Fig. 15. Measured and simulated ^{65}Zn profiles. Blue data points – the first measured profile, red data points – the second measured profile, orange line – the FLUKA-simulated profile, black dashed line – the energy-to-depth curve. The error bars represent statistical uncertainties provided by GammaVission. (For interpretation of the references to colour in this figure legend, the reader is referred to the web version of this article.)

Three different areas can be identified corresponding to different reaction mechanisms. At high projectile velocities the ^{65}Cu target nucleus can undergo a charge-exchange reaction replacing a neutron with a proton. This resulting increase by $\Delta Z = +1$ shows an increase of probability towards lower energy [46]. A sharp peak appears close to the end of the projectile range. Here more mechanisms can come in. A proton capture followed by a later neutron emission for deexcitation is possible within a limited energy range as it is well known for proton beams [47]. But it can as well occur as a part of a multi-nucleon transfer with a larger nucleus [48]. Finally, there is the long tail which is caused by the same interaction with light fragments of the Ar projectile. As the reaction requires only a proton as secondary projectile, the range of activation extends very far and drops only slowly by stopping of the heavier fragments or scattering of the lighter. The model in FLUKA predicts all three features, however, with less build-up effect at high velocity and a wider peak at the end of the range.

3.3.5. Reaction products heavier than the target

The experiments presented in [44] used ≈100 MeV/u $^{40}Ar^{17+}$ beam incident on Be and Ta targets. Reaction products of ^{36}Al, ^{37,38}Si, ^{38,39}P with enhanced neutron number and $^{37–40}$K with enhanced proton number were detected in case of Be and Ta targets, respectively. This cannot be explained by fragmentation but requires a charge exchange and fragmentation or direct multi-nucleon transfer. This is especially true for heavier target fragments we have observed, namely ^{75}Se, ^{83}Rb, ^{88}Y, and ^{88}Zr that were detected in two foils only. These foils are located at the projectile range at energies where such multi-nucleon transfer is possible. Multi-nucleon transfer was first investigated by implementation in stacked foils [49]. This phenomenon can be used as a projectile-range verification technique. This work is still in progress and is going to be treated in a separate paper. Nevertheless, we have already published some works on a similar topic [20,23].

3.4. Discussion

In addition to comparison of the measured and simulated depth-profiles by visual inspection of the graphs, we have adopted the criteria introduced in Ref. [38]. For each measured data point, the C/M ratio has been calculated and the number of the C/M ratios falling within three intervals has been counted. The C/M ratio stands for the ratio of the calculated (simulated) and measured values at a given depth of the profile. Results are collected in Table 4.

It can be seen that the worst FLUKA prediction is for light target fragments (^{7}Be), where the whole profile is underestimated by FLUKA. The maximum and minimum C/M ratio for ^{7}Be is 0.81 and 0.22, respectively. At the same time, this FLUKA profile also exhibits the most pronounced shape irregularity at the projectile energies from about 140 MeV/u down to about 60 MeV/u. The ^{22}Na profile is predicted by FLUKA quite well, but its measured projectile-fragment part is shifted slightly deeper with respect to the simulated one. The scoring according to Table 4 improves with increasing target-fragment mass until ^{57}Co that is the best case. There are more cases when FLUKA underestimates the activation (^{46}Sc, ^{54}Mn, ^{58}Co, ^{60}Co, ^{65}Zn) than the cases when FLUKA overestimates it (^{56}Co). Maximum and minimum C/M ratio is 1.7 and 0.08, respectively.

The overal scoring of 65.1% has been achieved in case of all nuclides average from the 1st and the 2nd data set for $0.7 < C/M < 1.3$ (488 "points in" out of the total 750 points, see Table 4). This is just slightly worse than the scoring of 71.4% reported in Ref. [38]. We have also observed similar trend of underestimating the induced activity by FLUKA. However, one has to take into account that the data in [38] have been collected for one particular type of nuclear reaction only, namely the ^{209}Bi(p, x) reactions. Moreover, the energy interval of the incident protons was also smaller, from 43 MeV to 100 MeV. In case of our experiment, the situation is much more complex including projectile and target fragmentation, different types of nuclear reactions, broader energy interval, and even different species of colliding particles due to production of secondary particles. Finally, proton is a less complex projectile compared to an argon nucleus. Keeping in mind this complexity, the agreement between FLUKA and the experiment is adequate. Nevertheless, the transition from RQMD to BME seems not to be smooth and suffers from artificial irregularities present in some of the simulated depth-profiles, most pronounced in the profile of ^{7}Be.

Generally, there is a good agreement between the first and the second sets of measurements. Let us remind that the spectrometric chain was recalibrated and the background measurement was repeated before

Table 4
The numbers of the C/M ratios are sorted into three intervals. The depth-profiles based on the first set of measurements consist of 46 data points each, the depth-profiles based on the second set of measurements consist of 48 data points each.

	0.9 < C/M < 1.1		0.8 < C/M < 1.2		0.7 < C/M < 1.3	
	1st set	2nd set	1st set	2nd set	1st set	2nd set
^{7}Be	0 (0%)	No data	1 (2%)	No data	3 (7%)	No data
^{22}Na	4 (9%)	2 (4%)	16 (35%)	13 (27%)	35 (76%)	27 (56%)
^{46}Sc	4 (9%)	Not used	20 (43%)	Not used	31 (67%)	Not used
^{54}Mn	9 (20%)	7 (15%)	27 (59%)	24 (50%)	43 (93%)	46 (96%)
^{56}Co	18 (39%)	21 (44%)	29 (63%)	31 (65%)	33 (72%)	34 (71%)
^{57}Co	30 (65%)	34 (71%)	40 (87%)	43 (90%)	46 (100%)	48 (100%)
^{58}Co	0 (0%)	0 (0%)	17 (37%)	7 (15%)	40 (87%)	41 (85%)
^{60}Co	0 (0%)	0 (0%)	1 (2%)	3 (6%)	16 (35%)	31 (65%)
^{65}Zn	3 (7%)	1 (2%)	5 (11%)	3 (6%)	7 (15%)	7 (15%)
All nuclides	68 (16%)	65 (19%)	156 (38%)	124 (37%)	254 (61%)	234 (70%)
	133 (18%)		280 (37%)		488 (65%)	

the second set of measurements. However, in case of the ^{46}Sc profile, the two sets of measurements do not coincide within 1σ statistical uncertainty. The second set of measurements is suffering from a systematic shift to higher values (see Fig. 8). We have investigated the possible causes of this shift. Analysis of the background spectrum revealed that there was a peak at 1120 keV in the background. There is also a possible influence from the ^{65}Zn photopeak at 1115.55 keV in the samples. The activity of ^{46}Sc during the second set of measurements was already quite low. For illustration, the first foil (0.5 mm thick) yielded about 1000 counts in the ^{46}Sc peaks per week. In case of the thinner foils (0.1 mm thick), the 889.28 ^{46}Sc keV peak was almost absent and the 1120.55 keV peak was overwhelmed to large extent by the background line of ^{214}Bi (1120.29 keV, 14.90% abundance). We did try to reprocess the ^{46}Sc second set spectra using some manual changes to the GammaVission settings, but minor improvement has only been achieved. Due to the low activity of the ^{46}Sc second set of measurements, we find this profile not reliable enough. That is why we have excluded it from the analysis presented in Table 4.

4. Conclusions

The paper presents original experimental data on 200 MeV/u ^{40}Ar fragmentation in a stacked-foil copper target. The fine target depth-resolution made a detailed comparison of measured and FLUKA-simulated depth-profiles possible. Although the overall agreement between the experiment and simulations is adequate and consistent with the results published elsewhere [38], some discrepancies have been observed. The FLUKA-simulated profiles differ from the measured ones especially for light target fragments, in our particular experiment represented by ^{7}Be. In most cases, FLUKA underestimates the target activation. There are also physically unjustified shape irregularities in the FLUKA-simulated profiles. Most of them can be observed at the projectile energies below 140 MeV/u, which might be caused by the transition from the Relativistic Quantum Molecular Dynamics to the Boltzmann Master Equation physical models. Depth-profiles of the nucleon-pickup target fragments showed that cross sections for nucleon pickup are small at high energies and increase rapidly with decreasing energy. This phenomenon could be used as a projectile-range verification technique (work in progress).

The presented experimental results could serve for further development and improvements to the Monte Carlo particle tracking codes like FLUKA.

CRediT authorship contribution statement

Edil Mustafin: Conceptualization, Methodology, Software, Validation, Formal analysis, Investigation, Resources, Data curation, Writing – review & editing, Visualization, Supervision, Project administration, Funding acquisition. **Peter Katrík:** Methodology, Validation, Investigation, Resources, Data curation, Writing – review & editing, Visualization. **Mários Pavlovič:** Conceptualization, Methodology, Validation, Writing – original draft, Writing – review & editing, Visualization. **Helmut Weick:** Conceptualization, Methodology, Software, Validation, Formal analysis, Investigation, Resources, Data curation, Writing – review & editing, Visualization, Supervision.

Declaration of Competing Interest

The authors declare that they have no known competing financial interests or personal relationships that could have appeared to influence the work reported in this paper.

Data availability

Data will be made available on request.

Acknowledgement

The results presented here are based on the experiment S451 that was performed at the HHD-cave at the GSI Helmholtzzentrum für Schwerionenforschung, Darmstadt (Germany) in the frame of FAIR Phase-0. Mários Pavlovič acknowledges partial funding from the Slovak Research and Development Agency by grant No. APVV-18-0243, and Scientific Grant Agency by grant No. VEGA 2/0084/20.

References

[1] S. Fujita, H. Tenzo, K. Takahashi, T. Sasaki, T. Kikuchi, Radiation damage in particle accelerator complex for heavy ion inertial fusion, High Energy Density Phys. 37 (2020), https://doi.org/10.1016/j.hedp.2020.100848.
[2] Š. Michalik, J. Michaliková, M. Pavlovič, P. Sovák, Hanns-Peter Liermann, M. Miglierini, Structural modifications of swift-ion-bombarded metallic glasses studied by high-energy X-ray synchrotron radiation, Acta Mater. 80 (2014) 309–316, https://doi.org/10.1016/j.actamat.2014.07.072.
[3] M. Pavlovič, M. Miglierini, E. Mustafin, W. Ensinger, A. Šagátová, M. Šoka, Radiation damage studies of soft magnetic metallic glasses irradiated with high-energy heavy ions, Radiat. Effects Defects in Solids: Incorporating Plasma Science and Plasma Technology 170 (1) (2015) 1–6, https://doi.org/10.1080/10420150.2014.993635.
[4] S. Michalik, M. Cesnek, M. Pavlovič, M. Miglierini, The effects of swift Xe ion bombardment on the amorphous structure of a VITROPERM type alloy, J. Alloy. Compd. 795 (2019) 69–78, https://doi.org/10.1016/j.jallcom.2019.04.328.
[5] U.H. Hossain, T. Seidl, W. Ensinger, Combined in situ infrared and mass spectrometric analysis of high-energy heavy ion induced degradation of polyvinyl polymers, Polym. Chem. 5 (3) (2014) 1001–1012, https://doi.org/10.1039/c3py01062g.
[6] T. Seidl, A. Plotnikov, E. Mustafin, R. Lopez, D. Severin, E. Floch, C. Trautmann, A. Golubev, A. Smolyakov, D. Tommasini, W. Ensinger, Influence of swift heavy ion beams and protons on the dielectric strength of polyimide, Polym. Degrad. Stab. 97 (11) (2012) 2396–2402, https://doi.org/10.1016/j.polymdegradstab.2012.07.025.
[7] T. Ogawa, M.N. Morev, T. Iimoto, T. Kosako, Measurements of induced activity in concrete by secondary particles at forward direction produced by intermediate energy heavy ions on an Fe target, Nucl. Instrum. Methods Phys. Res. Sect. B - Beam Interact. Mater. Atoms 269 (17) (2011) 1929–1939, https://doi.org/10.1016/j.nimb.2011.05.031.
[8] P. Spiller, P., Franchetti, G., The FAIR accelerator project at GSI, Nucl. Instrum. Methods Phys. Res. A, 561, 2 (2006) 305-309, DOI: 10.1016/j.nima.2006.01.043.
[9] M. Steck, C. Dimopoulou, A. Dolinskii, O. Gorda, V. Gostishchev, K. Knie, S. Litvinov, F. Nolden, C. Peschke, D. Obradors-Campos, Status of the Design of the FAIR Storage Rings, Int. J. Modern Phys. E 18 (2) (2009) 411–419.
[10] Boine-Frankenheim, O., "The FAIR Accelerators: Highlights and Challenges", In: Proceedings of the 1st International Particle Accelerator Conference, IPAC 2010, Kyoto, Japan (23-28 May 2010) 2430-2434, Code 100155, ISBN: 978-929083352-9.
[11] I. Strašík, E. Kozlova, E. Mustafin, A. Smolyakov, N. Sobolevsky, L. Latysheva, M. Pavlovič, Simulation of the residual activity induced by high-energy heavy ions, Nucl. Technol. 168 (2009) 643–647, https://doi.org/10.13182/NT09-A9282.
[12] I. Strašík, E. Mustafin, M. Pavlovič, Residual activity induced by heavy ions and beam-loss criteria for heavy-ion accelerators, Phys. Rev. Spec. Top. Accel Beams 13 (2010), https://doi.org/10.1103/PhysRevSTAB.13.071004.
[13] Mustafin, E., Iwase, H., Kozlova, E., Schardt, D., Fertman, A., Golubev, A.V, Hinca, R., Pavlovič, M., "Measured Residual Activity Induced by U Ions with Energy 500 MeV/u in Cu Target", Proceedings of EPAC2006: 10th European Particle Accelerator Conference. Edinburgh, 26.-30.6.2006, 2006, 1834-1836.
[14] A. Fertman, E. Mustafin, R. Hinca, I. Strašík, M. Pavlovič, D. Schardt, N. Sobolevsky, A.V. Golubev, B. Sharkov, G. Fehrenbacher, I. Hofmann, H. Iwase, E. Kozlova, G. Mustafina, First Results of an Experimental Study of the Residual Activity Induced by High-Energy Uranium Ions in Steel and Copper, Nucl. Instrum. Methods Phys. Res. Sect. B - Beam Interact. Mater. Atoms 260 (2007) 579–591, https://doi.org/10.1016/j.nimb.2007.03.077.
[15] I. Strašík, E. Mustafin, A. Fertman, R. Hinca, M. Pavlovič, D. Schardt, N. Sobolevsky, A.V. Golubev, B. Sharkov, G. Fehrenbacher, I. Hofmann, H. Iwase, E. Kozlova, G. Mustafina, "Experimental Study of the Residual Activity Induced by 950 MeV/u Uranium Ions in Stainless Steel and Copper, Nucl. Instrum. Methods Phys. Res. Sect. B - Beam Interact. Mater. Atoms 266 (2008) 3443–3452, https://doi.org/10.1016/j.nimb.2008.05.013.
[16] E. Mustafin, T. Seidl, A. Plotnikov, I. Strašík, M. Pavlovič, M. Miglierini, S. Stanček, A. Fertman, A. Lančok, Ion irradiation studies of construction materials for high-power accelerators, Radiat Eff. Defects Solids 164 (7–8) (2009) 460–469, https://doi.org/10.1080/10420150902949894.
[17] E. Kozlova, I. Strašík, A. Fertman, E. Mustafin, T. Radon, R. Hinca, M. Pavlovič, G. Fehrenbacher, H. Geissel, A.V. Golubev, H. Iwase, D. Schardt, Benchmark Test of the FLUKA Monte Carlo Code for Residual Production with 500 and 950 MeV/u Uranium Beams on Copper and Stainless Steel Targets, Nucl. Technol. 168 (2009) 747–751, https://doi.org/10.13182/NT09-A9300.
[18] I. Strašík, E. Mustafin, T. Seidl, M. Pavlovič, Experimental study and simulation of the residual activity induced by high-energy argon ions in copper, Nucl. Instrum.

Methods Phys. Res. Sect. B - Beam Interact. Mater. Atoms 268 (2010) 573–580, https://doi.org/10.1016/j.nimb.2009.12.004.
[19] V. Chetvertkova, I. Strašík, A. Belousov, H. Iwase, N. Mokhov, E. Mustafin, L. Latysheva, M. Pavlovič, U. Ratzinger, N. Sobolevsky, Activation of Aluminum by Argon: Experimental Study and Simulations, Nucl. Instrum. Methods Phys. Res. Sect. B - Beam Interact. Mater. Atoms 269 (2011) 1336–1340, https://doi.org/10.1016/j.nimb.2011.03.017.
[20] Strašík, I., Chetvertkova, V., Mustafin, E., Pavlovič, M., Belousov, A., Depth profiling of residual activity of ^{237}U fragments as a range verification technique for ^{238}U primary ion beam, Phys. Rev. Spec. Top. - Accelerators Beams 15 (2012) 071001-1, 071001-13, DOI: 10.1103/PhysRevSTAB.15.071001.
[21] P. Katrík, E. Mustafin, D.H. Hoffmann, M. Pavlovič, I. Strašík, Activation of accelerator construction materials by heavy ions, Nucl. Instrum. Methods Phys. Res. Sect. B - Beam Interact. Mater. Atoms 365 (2015) 525–528, https://doi.org/10.1016/j.nimb.2015.09.022.
[22] P. Katrík, D.H.H. Hoffmann, E. Mustafin, I. Strašík, Experimental study of residual activity induced in aluminium targets irradiated by high-energy heavy-ion beams: A comparison of experimental data and FLUKA simulations, Matter Radiat. Extremes 4 (5) (2019), https://doi.org/10.1063/1.5097035.
[23] E. Mustafin, P. Katrík, M. Pavlovič, Depth-profiling of activity induced by 300 MeV/u 124Xe ions in aluminum: ranges of heavy projectiles fragments, Nucl. Instrum. Methods Phys. Res. Sect. B - Beam Interact. Mater. Atoms 504 (2021) 33–42, https://doi.org/10.1016/j.nimb.2021.07.015.
[24] Battistoni, G. et al. "The FLUKA code: An Accurate Simulation Tool for Particle Therapy", Frontiers in Oncology 6 (11 May 2016) Article number 116, DOI: / 10.3389/fonc.2016.00116.
[25] Battistoni, G., Ferrari, A., Lantz, M. et al.: "A neutrino-nucleon interaction generator for the FLUKA Monte Carlo code", In: Proceedings of 12th International Conference on Nuclear Reaction Mechanisms, Varenna, Italy (15-19 June 2009) CERN-Proceedings-2010-001, 387-394.
[26] Battistoni, G., Boehlen, T., Cerutti, F., Chin, M.P.W., Esposito, L.S., FASSÒ, A., Ferrari, A., Lechner, A., Empl, A., Mairani, A., Mereghetti, A., Ortega, P.G., Ranft, J., Roesler, S., Sala, P.R., Vlachoudis, V., Smirnov, G.: "Overview of the FLUKA code", Annals of Nuclear Energy, 82 (2015) 10–18, https://doi.org/10.1016/j.anucene.2014.11.007.
[27] T.T. Böhlen, F. Cerutti, M.P.W. Chin, A. Fassò, A. Ferrari, P.G. Ortega, A. Mairani, P.R. Sala, G. Smirnov, V. Vlachoudis, The FLUKA Code: developments and challenges for high energy and medical applications, Nucl. Data Sheets 120 (2014) 211–214, https://doi.org/10.1016/j.nds.2014.07.049.
[28] H. Yashima, H., Uwamino, Y., Sugita, H., Ito, S., Nakamura, T., Fukumura, A.: Induced radioactivity in Cu targets produced by high-energy heavy ions and the corresponding estimated photon dose rates, Radiat. Protect. Dosimetry, 112, 2 (2004) 195–208, DOI: 10.1093/rpd/nch386.
[29] Mokhov, N.V., Striganov, S.I.: "MARS15 overview", In: ALBROW, M., RAJA, R. (eds.), Proceeding of the Hadronic Shower Simulation Workshop, Batavia, IL, 06-08 September 2006, Hadronic Shower Simulation Workshop, AIP Conference Proceedings (Book Series), 896 (2007), ISSN: 0094-243X, American Institute of Physics, 2 Huntington Quadrangle, STE 1NO1, Melville, NY 11747-4501, USA.
[30] Mokhov, N.V., Gudima, K.K., James, C.C., Kostin, M.A., Mashnik, S.G., NG, E., Ostiguy, J.-F., Rakhno, I.L., Sierk, A.J., Striganov, S.I.: "Recent enhancements to the MARS15 code, Radiat. Protect. Dosimetry 116 (1-4) (2005) 99–103, https://doi.org/10.1093/rpd/nci106.
[31] M.A. Kostin, N.V. Mokhov, Parallelising the MARS15 code with MPI for shielding applications, Radiat. Prot. Dosim. 116 (1–4) (2005) 297–300, https://doi.org/10.1093/rpd/nci006.
[32] N.V. Mokhov, K.K. Gudima, S.G. Mashnik, I.L. Rakhno, S.I. Striganov, Towards a heavy-ion transport capability in the MARS 15 code, Radiat. Prot. Dosim. 116 (1–4) (2005) 104–108, https://doi.org/10.1093/rpd/nci147.
[33] A. Grebe, A. Leveling, T. Lu, N. Mokhov, V. Pronskikh, The MARS15-based FermiCORD code system for calculation of the accelerator-induced residual dose, Nucl. Instrum. Methods Phys. Res., Sect. A 877 (2018) 339–345, https://doi.org/10.1016/j.nima.2017.08.055.
[34] Allison, J. et al.: Geant4 developments and applications, IEEE Trans. Nucl. Sci., 53, 1, Part: 2 (2006) 270-278, DOI: 10.1109/TNS.2006.869826.
[35] S. Agostinelli, et al., Geant4—a simulation toolkit, Nucl. Instrum. Methods Phys. Res., Sect. A 506 (3) (2003) 250–303, https://doi.org/10.1016/S0168-9002(03)01368-8.
[36] L. Sihver, T. Sato, K. Gustafsson, D. Mancusi, H. Iwase, K. Niita, H. Nakashima, Y. Sakamoto, Y. Iwamoto, N. Matsuda, An update about recent developments of the PHITS code, Adv. Space Res. 45 (7) (2010) 892–899, https://doi.org/10.1016/j.asr.2010.01.002.
[37] A.V. Dementyev, N.M. Sobolevsky, SHIELD — universal Monte Carlo hadron transport code: scope and applications, Radiat. Meas. 30 (5) (1999) 553–557, https://doi.org/10.1016/S1350-4487(99)00231-0.
[38] Leila Mokhtari Oranj, Mahdi Bakhtiari, Yong-Uk Kye, Nam-Suk Jung, Arim Lee, Hee-Seock Lee, Benchmarking FLUKA, PHITS, MCNPX, and MARS15 codes with product yields of ^{209}Bi(p, x) reactions, Nucl. Instrum. Methods Phys. Res. Sect. B 462 (2020) 154-162, https://doi.org/10.1016/j.nimb.2019.11.017.
[39] Bozyk, L., Spiller, P., Kollmus, H.: Development of a Cryocatcher-System for SIS100, Proceedings of IPAC2012, May 20-25, 2012, New Orleans, Louisiana, USA, ISBN 978-3-95450-115-1, THEPPB004, 3237-3239. [Available at https://accelconf.web.cern.ch/ipac2012/papers/theppb004.pdf, last access on the 12th of December 2021.].
[40] Weick, H., Geissel, H., Iwasa, N., Scheidenberger, C., Rodriguez SANCHEZ, J.L., Prochazka, A., Purushotaman, S: Improved accuracy of the code ATIMA for energy loss of heavy ions in matter, In: GSI Scientific Report 2017, GSI Report 2018-1 (November 2018) 130-131, DOI: 10.15120/GR-2018-1. [energy-loss calculator available at https://www.isotopea.com/webatima, last access on 4th of January 2022].
[41] Ferrari, A., Sala, P.R., Fassò, A., Ranft, J.: FLUKA: a multi-particle transport code (Program version 2021), CERN-2005-010 INFN TC 05/11 SLAC-R-773 Revision 150, Milan, December 16th, 2021. [Available at http://www.fluka.org/content/manuals/FM.pdf, last download on the 3rd of May 2022.].
[42] N. Iwasa, H. Geissel, G. Munzenberg, C. Scheidenberger, T. Schwab, H. Wollnik, Mocadi, a universal Monte Carlo code for the transport of heavy ions through matter within ion-optical systems, Nucl. Instrum. Methods Phys. Res., Sect. B 126 (1–4) (1997) 284–289, https://doi.org/10.1016/S0168-583X(97)01097-5.
[43] J.B. Cumming, P.E. Haustein, H.C. Hseuh, Momentum-transfer in the fragmentation of Cu by relativistic heavy-ions and protons, Phys. Rev. C 24 (5) (1981) 2162–2173, https://doi.org/10.1103/PhysRevC.24.2162.
[44] M. Notani, et al., Projectile fragmentation reactions and production of nuclei near the neutron drip line, Phys. Rev. C 76 (4) (2007), 044605, https://doi.org/10.1103/PhysRevC.76.044605.
[45] J.J. Gaimard, K.-H. Schmidt, A reexamination of the abrasion-ablation model for the description of the nuclear fragmentation reaction, Nucl. Phys. A 531 (3–4) (1991) 709–745, https://doi.org/10.1016/0375-9474(91)90748-U.
[46] J.R. Cummings, W.R. Binns, T.L. Garrard, M.H. Israel, J. Klarmann, E.C. Stone, C. J. Waddington, Determination of the cross sections for the production of fragments from relativistic nucleus-nucleus interactions. I. Measurements, Phys. Rev. C 42 (6) (1990) 2508–2529, https://doi.org/10.1103/PhysRevC.42.2508.
[47] P. Kopecký, Proton-beam monitoring via the Cu(p, X)Co-58, Cu-63(p, 2n)Zn-62 and Cu-65(p, n)Zn-65 reactions in copper, Int. J. Appl. Radiat. Isot. 36 (8) (1985) 657–661, https://doi.org/10.1016/0020-708X(85)90008-0.
[48] L. Corradi, et al., Multinucleon transfer reactions: Present status and perspectives, Nucl. Instrum. Methods Phys. Res., Sect. B 317 (15) (2013) 743–751, https://doi.org/10.1016/j.nimb.2013.04.093.
[49] R. Kaufmann, R. Wolfgang, Nucleon transfer reactions in grazing collisions of heavy ions, Phys. Rev. 121 (1) (1961) 192–205, https://doi.org/10.1103/PhysRev.121.192.